

Calibrating the binary black hole population in nuclear star clusters through tidal disruption events

Giacomo Fragione^{1,2*}, Rosalba Perna^{3,4}, Abraham Loeb⁵

¹*Department of Physics & Astronomy, Northwestern University, Evanston, IL 60202, USA*

²*Center for Interdisciplinary Exploration & Research in Astrophysics (CIERA), Evanston, IL 60202, USA*

³*Department of Physics and Astronomy, Stony Brook University, Stony Brook, NY 11794-3800, USA*

⁴*Center for Computational Astrophysics, Flatiron Institute, New York, NY 10010, USA*

⁵*Astronomy Department, Harvard University, 60 Garden St., Cambridge, MA 02138, USA*

9 November 2020

ABSTRACT

As the sensitivity of gravitational wave (GW) instruments improves and new networks start operating, hundreds of merging stellar-mass black holes (SBHs) and intermediate-mass black holes (IMBHs) are expected to be observed in the next few years. The origin and distribution of SBH and IMBH binaries in various dynamical environments is a fundamental scientific question in GW astronomy. In this paper, we discuss ways tidal disruption events (TDEs) may provide a unique electromagnetic window into the assembly and merger of binary SBHs and IMBHs in nuclear star clusters (NSCs). We discuss how the host NSC mass and density and the slope of the black-hole mass function set the orbital properties and the masses of the binaries that undergo a TDE. For typical NSC properties, we predict a TDE rate of $\sim 10^{-6}$ – 10^{-7} yr⁻¹ per galaxy. The lightcurve of TDEs in NSCs could be interrupted and modulated by the companion black hole on the orbital period of the binary. These should be readily detectable by optical transient surveys such as the Zwicky Transient Facility and LSST.

Key words: stars: black holes – galaxies: kinematics and dynamics – stars: black holes – stars: kinematics and dynamics – galaxies: nuclei

1 INTRODUCTION

Ten binary stellar-mass black holes (SBHs) and one binary neutron star (NS) have been detected through their gravitational wave (GW) emission during the first and second observing runs of LIGO/Virgo¹ (LIGO/Virgo Scientific Collaboration 2019a). The third run has already revealed the merger of a binary NS of $\sim 3.4 M_{\odot}$ (LIGO/Virgo Scientific Collaboration 2020b), the most massive ever observed, and the merger of a binary SBH with a low-mass ratio and high spin (LIGO/Virgo Scientific Collaboration 2020a). The merger rate in the local Universe has been estimated to be in the ranges ~ 9.7 – 101 Gpc⁻³ yr⁻¹ and ~ 250 – 2810 Gpc⁻³ yr⁻¹ for binary SBH and NS, respectively. No SBH-NS binaries have been confirmed, with a LIGO/Virgo 90% upper limit of ~ 610 Gpc⁻³ yr⁻¹ on the merger rate (LIGO/Virgo Scientific Collaboration 2019a).

Many astrophysical scenarios have been proposed to explain the mergers observed via GW emission by the

LIGO/Virgo collaboration. Possibilities include isolated binary evolution (Belczynski et al. 2016; Giacobbo & Mapelli 2018; Kruckow et al. 2018), mergers in star clusters (Askar et al. 2017; Banerjee 2018; Fragione & Kocsis 2018a; Rodriguez et al. 2018; Samsing 2018; Di Carlo et al. 2019; Perna et al. 2019; Kremer et al. 2020; Di Carlo et al. 2020), mergers in galactic nuclei (O’Leary et al. 2009; Antonini & Perets 2012; Fragione et al. 2019; Grishin et al. 2018; Hamilton & Rafikov 2019; Rasskazov et al. 2019), mergers in gaseous disks (Bartos et al. 2017; Tagawa et al. 2019), and Lidov-Kozai (LK) mergers in isolated triple and quadruple systems (Antonini et al. 2017; Silsbee & Tremaine 2017; Fragione & Kocsis 2019; Hamers & Thompson 2019; Liu & Lai 2019).

Merger of black holes of $\sim 10^2 M_{\odot}$ – $10^5 M_{\odot}$, in the regime of intermediate-mass black holes (IMBHs), could also be detected by GW instruments. At design sensitivity, LIGO/Virgo, the Einstein Telescope² (ET), DECIGO³

* E-mail: giacomo.fragione@northwestern.edu

¹ <http://www.ligo.org>

² <http://www.et-gw.eu>

³ https://decigo.jp/index_E.html

and LISA⁴, will be able to detect GW sources from merging IMBHs of masses up to $\sim 100 - 1000 M_{\odot}$, $\sim 10^3 - 10^4 M_{\odot}$ and $\gtrsim 10^4 M_{\odot}$, respectively (e.g., [Amaro-Seoane et al. 2007](#); [Fragione et al. 2018](#); [Bellovary et al. 2019](#)). Using the non-detection of massive binaries in the first two observational runs, the LIGO/Virgo collaboration placed upper limits on merging IMBHs of the order of $\sim 0.1-1 \text{ Gpc}^{-3} \text{ yr}^{-1}$ ([LIGO/Virgo Scientific Collaboration 2019b](#)).

Mergers of binaries where one or both components are IMBHs can occur in a variety of environments. Unlike the SBH case, binaries hosting an IMBH cannot be produced by the collapse of stars in a canonical binary evolution, except for the case of Pop III stars ([Madau & Rees 2001](#); [Bromm & Larson 2004](#); [Fryer et al. 2001](#); [Bromm 2013](#); [Loeb & Furlanetto 2013](#)). Therefore, dynamical scenarios are generally favored, representing the ideal place where an IMBH can find a SBH/NS/IMBH companion to merge with. These environments include nuclear star clusters ([Mastrobuono-Battisti et al. 2014](#); [Fragione & Leigh 2018a](#); [Antonini et al. 2019](#)), globular clusters ([Mandel et al. 2008](#); [Fragione et al. 2018](#); [Rasskazov et al. 2019](#); [Kremer et al. 2020](#)), and active galactic nuclei (AGN) accretion disks ([McKernan et al. 2012, 2014](#)).

As the sensitivity of current GW detectors improves and new networks start operating, hundreds of merging SBHs are expected to be detected over the next few years ([LIGO/Virgo Scientific Collaboration 2019a](#)). While low-mass IMBHs could already be observed by LIGO/Virgo ([LIGO/Virgo Scientific Collaboration 2019b](#)), the majority of IMBHs merging in binary systems are expected to be detected with the upcoming ET, DECIGO, and LISA missions ([Miller 2009](#)). Therefore, the origin and distribution of SBH and IMBH binaries in dynamical environments is a key scientific question that will be addressed with future GW data.

In this paper we discuss the electromagnetic window, provided by tidal disruption events (TDEs) of stars, into the assembly and merger history of binary SBHs and IMBHs⁵ in nuclear star clusters (NSCs). In this environment the lightcurve of the TDEs can be interrupted and modulated by the companion BH on the orbital period of the binary (e.g., [Liu et al. 2009](#); [Coughlin et al. 2017](#); [Fragione et al. 2019](#)), which can then be used to probe the binary SBH and IMBH orbital period distribution ([Samsing et al. 2019](#)). We compute the rates of TDEs for various NSC masses and densities, and different distributions of the SBH and IMBH mass function. We also discuss the typical electromagnetic signal expected as a result of these events and how it can be used to detect binary BHs.

The paper is organized as follows. In Section 2, we describe the various channels that lead to the formation of binary BHs. In Section 3, we show how TDEs can be used to infer the characteristics of binary BHs in galactic nuclei, and compute the relative rates for a population of SBHs and IMBHs. In Section 4, we discuss the electromagnetic signatures of these events. Finally, in Section 5, we discuss the implications of our findings and draw our conclusions.

2 BLACK HOLE BINARIES IN NUCLEAR STAR CLUSTERS

Here we summarize the main mechanisms that can lead to the formation of hard SBH-SBH, IMBH-SBH, and IMBH-IMBH binaries in a given NSC. We label the mass and the density of the NSC M_{NSC} and ρ_{NSC} , respectively. We define the cluster velocity dispersion $\sigma = v_{\text{esc}}/(2\sqrt{3})$, where v_{esc} is the cluster escape speed ([Georgiev et al. 2009](#)),

$$v_{\text{esc}} = 40 \text{ km s}^{-1} \left(\frac{M_{\text{NSC}}}{10^5 M_{\odot}} \right)^{1/3} \left(\frac{\rho_{\text{NSC}}}{10^5 M_{\odot} \text{ pc}^{-3}} \right)^{1/6}. \quad (1)$$

Binary BHs can be formed through the interaction of three objects in the core of a NSC. Interactions come in two flavours: encounters between three single objects and encounters between a single and a binary (e.g., [Antonini & Rasio 2016](#); [Fragione & Silk 2020](#)). In the first case, BH binaries can be assembled through three-body processes in which a binary is formed with the help of a third BH, which carries away the excess energy needed to bind the pair (e.g., [Lee 1995](#)). In the second case, binary BHs can also form through exchange interactions, mediated initially by primordial stellar binaries. When a BH gets within a couple of semimajor axes lengths of a binary, it will tend to break the binary and to acquire a companion. After BH binaries are formed, they dominate the dynamics inside the cluster core (e.g. [Miller & Lauburg 2009](#)).

Another channel to form binary BHs in a NSC is gravitational bremsstrahlung. In this scenario, two single BHs pass sufficiently close to each other to dissipate enough energy via GW radiation to remain bound (e.g., [Turner 1977](#)). However, binary BHs formed through GW captures are typically very eccentric and merge within a few minutes up to a few years (depending on the BH masses) after formation ([O’Leary et al. 2009](#); [Rasskazov & Kocsis 2019](#); [Fragione et al. 2020](#)).

Star clusters are promising environments for forming binary BHs ([Askar et al. 2017](#); [Fragione & Kocsis 2018b](#); [Rodriguez et al. 2018](#)). For what concerns IMBHs, a number of studies have showed that the most massive stars may segregate and merge in the core of the cluster, forming a massive growing object that could collapse to form an IMBH ([Portegies Zwart & McMillan 2002](#); [Gürkan et al. 2004](#); [Giersz et al. 2015](#)). Binaries containing the IMBH can later be formed through three-body interactions ([Mandel et al. 2008](#); [Fragione & Bromberg 2019](#)). Star clusters born in the innermost galactic regions could have dynamical friction timescales small enough to efficiently inspiral into the centres of galaxies (e.g., [Tremaine et al. 1975](#); [Capuzzo-Dolcetta & Micocchi 2008](#); [Gnedin et al. 2014](#)). Any binary BH formed within these clusters could therefore be delivered to the innermost regions of the host galaxy (e.g., [Gürkan & Rasio 2005](#); [Mastrobuono-Battisti et al. 2014](#); [Arca-Sedda & Gualandris 2018](#); [Fragione et al. 2018](#)).

Binary BHs could also form efficiently in the gaseous disks of active galactic nuclei (AGN; [McKernan et al. 2012, 2014](#)). If migration traps are present in the gaseous disk surrounding a supermassive BH, differential gas torques exerted on the orbiting SBHs and IMBHs will cause them to migrate towards a migration trap ([Secunda et al. 2018](#)). Turbulence in the gaseous disk can knock orbiting SBHs out of resonance, allowing them to drift close to the trap

⁴ <https://lisa.nasa.gov>

⁵ In the following, we use BH to refer to either SBH or IMBH without distinction.

and experience a close interaction with other BHs. Since the interactions are dissipative due to the gas, it could be possible to form SBH-SBH, IMBH-SBH, and IMBH-IMBH binaries. Some of these objects could also merge repeatedly, thus forming massive BHs (McKernan et al. 2019; Yang et al. 2019).

We consider stars undergoing TDEs onto hard binaries that are formed through the interaction of initially unbound BHs. Hard binaries can be defined based on the softness parameter (Heggie 1975),

$$\eta = \frac{Gm_{\text{BH},1}m_{\text{BH},2}}{2a\langle m \rangle\sigma^2}, \quad (2)$$

where $m_{\text{BH},1}$ is the mass of the primary BH, $m_{\text{BH},2}$ ($m_{\text{BH},2} < m_{\text{BH},1}$) is the mass of the secondary BH, a and e the semi-major axis and eccentricity of the binary, respectively, and $\langle m \rangle$ and σ are the average star mass and the cluster velocity dispersion, respectively. Binaries with $\eta \ll 1$ are called soft binaries and will become even softer on average, until they are disrupted by interactions with other stars and compact objects; on the other hand, binaries with $\eta \gg 1$ are referred to as hard binaries and tend to become even harder (Heggie 1975). As a result of their interactions with other stars and compact objects, binaries formed at the hardening semi-major axis (Quinlan 1996),

$$a_{\text{hard}} = 2.5 \text{ AU} \left(\frac{m_{\text{BH},2}}{10 M_{\odot}} \right) \left(\frac{\sigma}{30 \text{ km s}^{-1}} \right)^{-2}, \quad (3)$$

tend to shrink at a constant rate (Quinlan 1996), eventually down to a separation,

$$a_{\text{GW}} = 0.05 \text{ AU} \left(\frac{m_{\text{BH},1} + m_{\text{BH},2}}{20 M_{\odot}} \right)^{3/5} \left(\frac{10^6 M_{\odot} \text{ pc}^{-3}}{\rho_{\text{NSC}}} \right)^{1/5} \times \left(\frac{\sigma}{30 \text{ km s}^{-1}} \right)^{1/5} \left(\frac{q}{(1+q)^2} \right)^{1/5}, \quad (4)$$

where GWs takes over and hence the binary merges. Note that during one of the interactions that makes the binary shrink, the binary itself can receive a dynamical kick such that it is ejected from the host NSC (Antonini & Rasio 2016).

3 TIDAL DISRUPTION EVENTS IN BINARY BLACK HOLES

More than $\sim 60\%$ of early- and late-type galaxies show observational evidence indicating that the nuclear regions of galaxies are occupied by a NSC and/or a central supermassive black hole. NSCs are present mainly in faint galaxies, while supermassive black holes are common in galaxies with masses $\gtrsim 10^{10} M_{\odot}$ (e.g., Capuzzo-Dolcetta & Tosta e Melo 2017). The most complete catalog of NSC can be found in the sample of Georgiev et al. (2016). This sample of NSCs comprises the systems in spheroid-dominated galaxies (Côté et al. 2006; Turner et al. 2012) and disc-dominated galaxies (Georgiev et al. 2009; Georgiev & Böker 2014). The masses and densities of the known NSCs are $10^4 M_{\odot} \lesssim M_{\text{NSC}} \lesssim 10^8 M_{\odot}$ and $10^4 M_{\odot} \text{ pc}^{-3} \lesssim \rho_{\text{NSC}} \lesssim 10^8 M_{\odot} \text{ pc}^{-3}$, respectively (see e.g. Fig. 1 in Fragione & Silk 2020).

We consider the fate of a star (assumed to have a solar mass, $m_* = 1 M_{\odot}$, and radius $R_* = 1 R_{\odot}$) that interacts

with a binary SBH-SBH, IMBH-SBH, or IMBH-IMBH during its lifetime in NSCs of various masses and densities. Table 1 summarizes the properties of the host NSC we consider in this work:

- The NSC mass and density are varied in the range $0.5 \leq M_{\text{NSC}}/10^7 M_{\odot} \leq 10$ and $1 \leq \rho_{\text{NSC}}/10^6 M_{\odot} \text{ pc}^{-3} \leq 50$, respectively.
- BH masses are sampled from a BH mass function, assumed for simplicity to follow a distribution

$$f(m_{\text{BH}}) \propto m_{\text{BH}}^{-\beta}, \quad (5)$$

where $1.0 \leq \beta \leq 4$. SBH masses are drawn in the interval $[5 M_{\odot}, 100 M_{\odot}]$, while IMBH masses in the interval $[10^2 M_{\odot}, 10^4 M_{\odot}]$.

- The initial BH binaries are assumed to be on a circular orbit of initial semi-major axis chosen either to be $a = a_{\text{hard}}$ (Mod1 and Mod2) or in the range $a_{\text{GW}} < a < a_{\text{hard}}$ (Mod3, Mod4, and Mod5).

- In the scattering experiments, the relative velocity of the binary and of the incoming star are fixed to the velocity dispersion σ of the host NSC, assumed to be roughly constant within the region of interest (Pechetti et al. 2020). The impact parameter is drawn from a distribution

$$f(b) = \frac{1}{2} \frac{b}{b_{\text{max}}^2}, \quad (6)$$

where b_{max} is the maximum impact parameter of the scattering experiment defined by

$$b_{\text{max}} = p_{\text{max}} \sqrt{1 + \frac{2GM_T}{p_{\text{max}}\sigma^2}}. \quad (7)$$

In the above equation, M_T is the total mass (binary+star) of the system and p_{max} is the maximum pericentre distance of the encounter. The initial separation of the binary and incoming star is chosen to be the distance at which the tidal perturbation on both systems has a fractional amplitude $\delta = F_{\text{tid}}/F_{\text{rel}} = 10^{-5}$. Here, F_{rel} and F_{tid} are the relative forces between the components of the binary and the initial tidal force between the binary and the star, respectively (Fregeau et al. 2004; Antognini & Thompson 2016).

- Two angles describe the relative orientations and phases of the encounter, given the plane of motion of the center of mass of the BH binary and of the star. The relative inclination of the orbital plane of the binary constitutes the first angle. The initial phases of the BHs in the binary add an additional angle. For all the scattering experiments, these angles are chosen randomly.

To run our scattering experiments, we use the FEWBODY numerical toolkit (Fregeau et al. 2004), which classifies the results of the scattering events into a set of independently bound hierarchies and considers a run completed when their relative energy is positive and the tidal perturbation on each outcome system is smaller than δ .

As discussed in Chen et al. (2009) and Chen et al. (2011) in the context of supermassive black hole binaries, close resonant encounters and secular effects of the stars that are trapped within the binary orbit can efficiently produce TDEs. To quantify the probability of TDEs, we define the cross section

$$\Sigma_{\text{TDE}} = \pi b_{\text{max}}^2 \hat{\Sigma}_{\text{TDE}}, \quad (8)$$

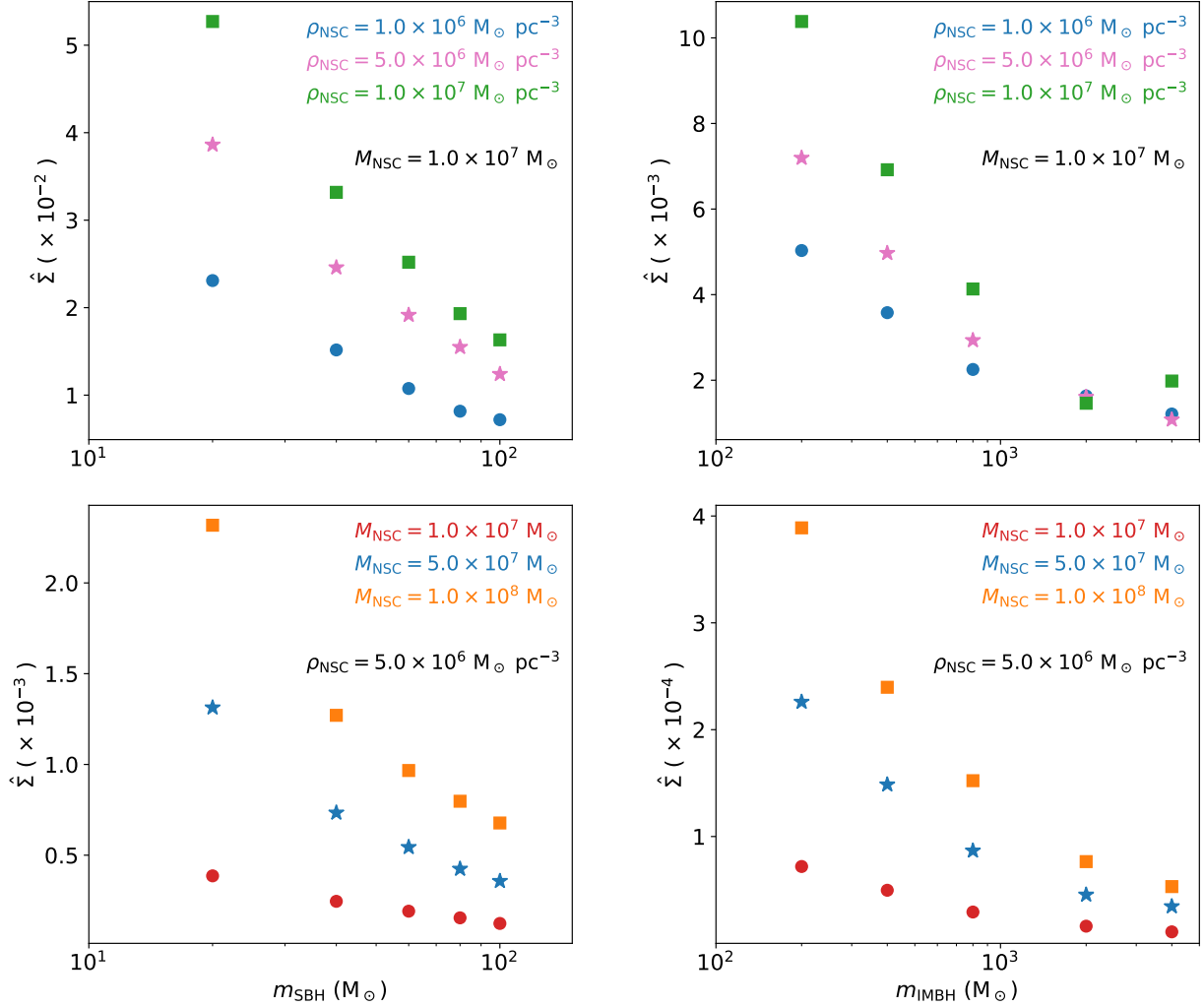


Figure 1. Left: branching ratio ($\hat{\Sigma}$) as a function of the SBH mass (m_{SBH}) for equal mass binaries at the hardening radius. Right: branching ratio as a function of the IMBH mass (m_{IMBH}) for equal mass binaries at the hardening radius. Top panel: $M_{\text{NSC}} = 10^7 M_{\odot}$ and different values of ρ_{NSC} ; bottom panel: $\rho_{\text{NSC}} = 5.0 \times 10^6 M_{\odot} \text{pc}^{-3}$ and different values of M_{NSC} .

where b_{max} is the maximum impact parameter and

$$\hat{\Sigma}_{\text{TDE}} = \frac{N_{\text{TDE}}}{N_{\text{tot}}} \quad (9)$$

is the branching ratio. Here, N_{TDE} is the number of scatterings that ends in a TDE, which is determined by the condition that the star passes within the tidal disruption radius

$$R_{\text{T}} = R_* \left(\frac{m_{\text{BH},i}}{m_*} \right)^{1/3}, \quad i = 1, 2 \quad (10)$$

of one of the BHs ($i = 1, 2$) in the binary, and N_{tot} is the total number of scattering experiments. In our simulations, we fix $b_{\text{max}} = 2a_{\text{hard}}$, since the stars that result in a TDE are the ones that can be effectively deflected and trapped in the binary BH orbit. For each model in Table 1, we run 10^5 scattering experiments.

Table 1. Model parameters: name, mass of the NSC (M_{NSC}), density of the NSC (ρ_{NSC}), slope of the black hole mass function (β).

Name	M_{NSC} ($10^7 M_{\odot}$)	ρ_{NSC} ($10^6 M_{\odot} \text{pc}^{-3}$)	β
Mod1	1	1-10	-
Mod2	1-10	5	-
Mod3	0.5-10	1	2.3
Mod4	0.5	1-50	2.3
Mod5	0.5	1	1.0-4.0

3.1 Dependence on the maximum black hole mass

In Mod1 and Mod2 (see Table 1), we consider scattering experiments of stars interacting with equal-mass binaries. We consider both SBH-SBH and IMBH-IMBH binaries. In order to estimate the role of the maximum BH mass, we fix the binary semi-major axis to the hardening semi-major axis a_{hard} (Eq. 3).

We plot in Figure 1 the branching ratio $\hat{\Sigma}$ as a function

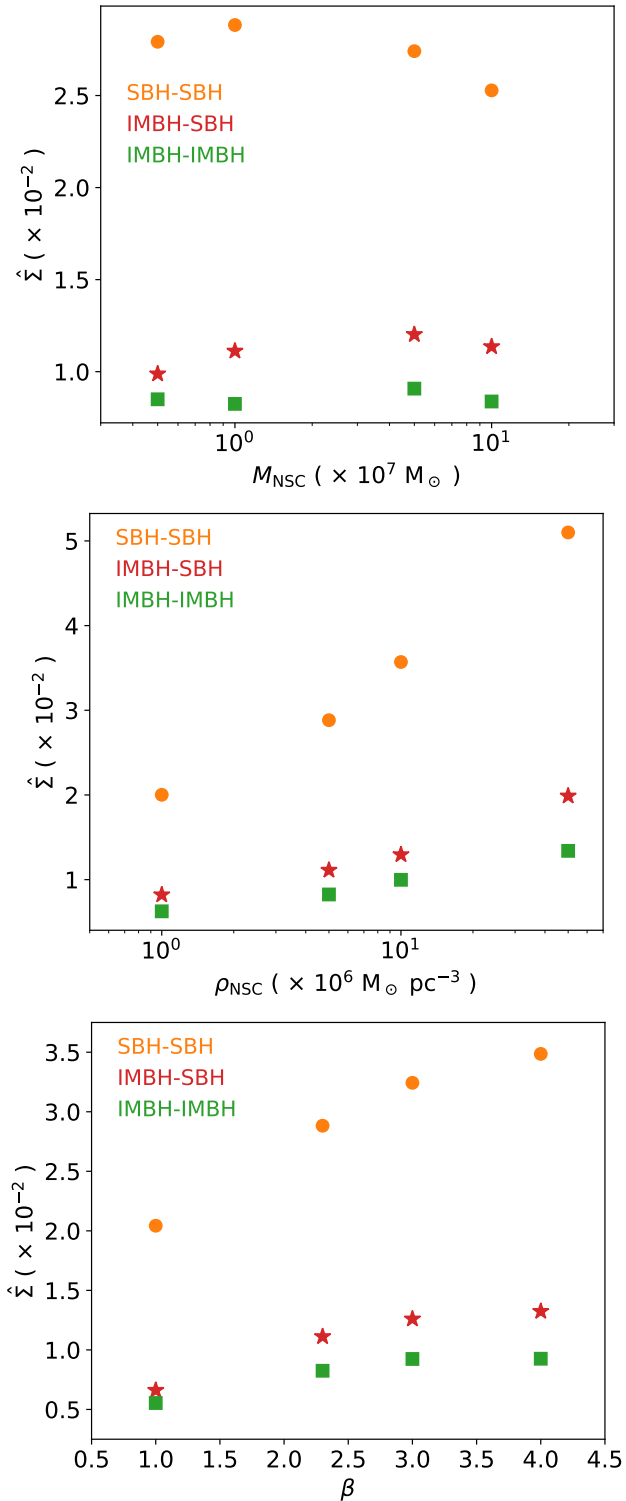


Figure 2. Top panel: branching ratio as a function of the NSC mass ($\rho_{\text{NSC}} = 5 \times 10^6 \text{ M}_\odot \text{ pc}^{-3}$, $\beta = 2.3$) for SBH-SBH (orange), IMBH-SBH (red), and IMBH-IMBH (green). Central panel: branching ratio as a function of the NSC density ($M_{\text{NSC}} = 10^7 \text{ M}_\odot$, $\beta = 2.3$) for SBH-SBH (orange), IMBH-SBH (red), and IMBH-IMBH (green). Bottom panel: branching ratio as a function of the slope of the BH mass function ($M_{\text{NSC}} = 10^7 \text{ M}_\odot$, $\rho_{\text{NSC}} = 5 \times 10^6 \text{ M}_\odot \text{ pc}^{-3}$) for SBH-SBH (orange), IMBH-SBH (red), and IMBH-IMBH (green).

of the SBH mass m_{SBH} (left panel) and as a function of the IMBH mass m_{IMBH} (right panel) for equal mass binaries. In the top panel we show the branching ratio for TDEs in the case the host NSC has mass $M_{\text{NSC}} = 10^7 \text{ M}_\odot$ and different densities, while in the bottom panel we show the branching ratio for TDEs in the case the host NSC has density $\rho_{\text{NSC}} = 5 \times 10^6 \text{ M}_\odot \text{ pc}^{-3}$ and different masses. In both cases, we find that $\hat{\Sigma}$ decreases for larger BH masses. Moreover, the branching ratio becomes larger for larger NSC masses and densities. These trends can be understood in terms of the scale of the hardening radius,

$$a_{\text{hard}} \propto \frac{m_{\text{BH}}}{\sigma^2} \propto \frac{m_{\text{BH}}}{M_{\text{NSC}}^{2/3} \rho_{\text{NSC}}^{1/3}}. \quad (11)$$

For fixed NSC mass and density, larger BH masses correspond to larger hardening radii; on the other hand, larger NSC masses and densities lead to larger hardening radii, at a fixed BH mass. While wider binaries can intercept a larger flux of incoming stars, the stars that lead to a TDE are the ones that, during resonant encounters, have the chance to pass within the tidal radius (see Eq. 10) of one of the two BHs (m_{BH}) and be tidally disrupted. As a result, the branching ratio is smaller for wider binaries, since it will be less probable for a star to pass close enough ($\lesssim R_{\text{T}}$) to one of the BHs during resonant encounters.

3.2 Dependence on NSC mass and density and slope of black hole mass function

In Mod3, Mod4, and Mod5, we consider a population of SBH-SBH, IMBH-SBH, IMBH-IMBH binaries to study the effect of the NSC mass, NSC density, and slope of the mass function. In these models, we consider binaries that are hard enough not to be ionized by encounters with other stars and compact objects ($a < a_{\text{hard}}$), but wide enough such that their dynamics is not dominated by GW emission ($a > a_{\text{GW}}$). To this end, we sample the semi-major axis of the interacting binary BHs from a log-uniform distribution in the interval $(a_{\text{GW}}, a_{\text{hard}})$. BH masses are sampled from a negative power law with exponent β .

We present the results of our scattering experiments in Figure 2, for SBH-SBH (orange), IMBH-SBH (red), and IMBH-IMBH (green) binaries. In the top panel we show $\hat{\Sigma}$ as a function of the NSC mass ($\rho_{\text{NSC}} = 5 \times 10^6 \text{ M}_\odot \text{ pc}^{-3}$, $\beta = 2.3$); in the central panel, we plot the branching ratio as a function of the NSC density ($M_{\text{NSC}} = 10^7 \text{ M}_\odot$, $\beta = 2.3$); in the bottom panel, we show $\hat{\Sigma}$ as a function of the slope of the BH mass function ($M_{\text{NSC}} = 10^7 \text{ M}_\odot$, $\rho_{\text{NSC}} = 5 \times 10^6 \text{ M}_\odot \text{ pc}^{-3}$). The general trend with a_{hard} discussed previously is in part smeared out by the fact that we sample the binary semi-major axis in the range $(a_{\text{GW}}, a_{\text{hard}})$, rather than having it fixed to a_{hard} . Moreover, BHs do not have a fixed mass, as in Mod1 and Mod2 in equal-mass binaries, but their masses are sampled from a distribution. Additionally, we find that SBH-SBH binaries produce the largest branching ratio, while IMBH-IMBH lead to the lowest one. This can again be ascribed to the fact that hard binaries of two SBHs have typically smaller semi-major axes than binaries comprised of two IMBHs. As a consequence, stars that undergo a resonant encounter with an SBH-SBH binary are more likely to pass within the tidal radius of one of the two BHs and get tidally disrupted. Branching ratios of binary

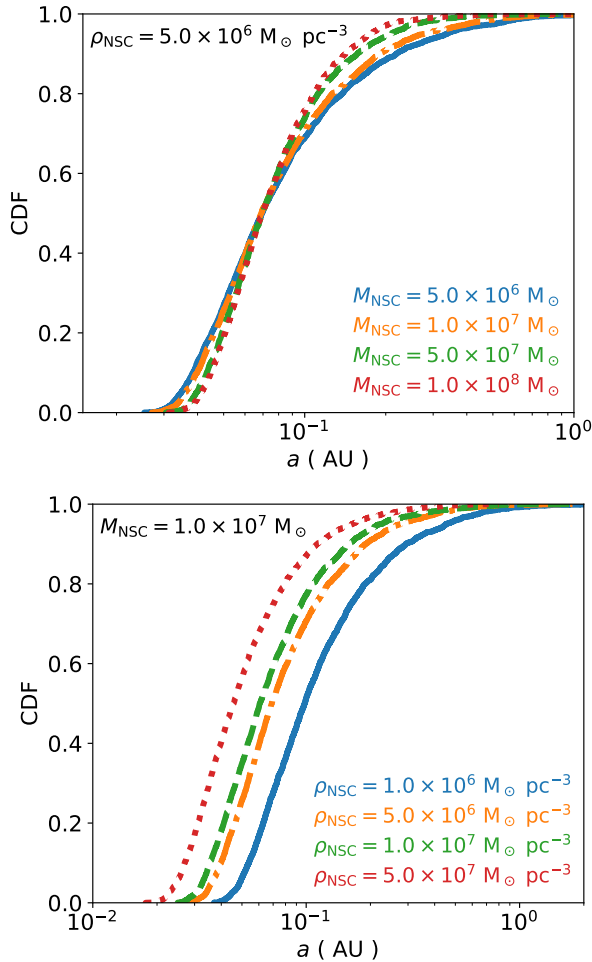


Figure 3. Distribution of semi-major axis (a) of the SBH-SBH binaries that undergo a TDE. Top panel: $\rho_{\text{NSC}} = 5 \times 10^6 M_{\odot} \text{pc}^{-3}$ and different values of the NSC mass; bottom panel: $M_{\text{NSC}} = 10^7 M_{\odot}$ and different values of the NSC density. The slope of the SBH mass function is fixed to $\beta = 2.3$.

IMBH-SBHs are in between the SBH-SBH and IMBH-SBH cases.

3.3 Orbital properties of binaries that exhibit tidal disruption events

The semi-major axis of the binaries that undergo a TDE depends on the host NSC mass and density, and on the slope of the BH mass function β .

We illustrate in Figure 3 the distribution of semi-major axes of the SBH-SBH binaries that undergo a TDE. In the top panel, we show the case for $\rho_{\text{NSC}} = 5 \times 10^6 M_{\odot} \text{pc}^{-3}$ and different values of the NSC mass (Mod3), while in the bottom panel, we plot the case for $M_{\text{NSC}} = 10^7 M_{\odot}$ and different values of the NSC density (Mod4). The slope of the SBH mass function is fixed at $\beta = 2.3$. We find that the NSC mass has only a modest effect in shaping the semi-major axis of the binaries that undergo a TDE, unlike the host NSC density. The reason for this trend can be explained considering that binaries have orbital semi-major axis in the

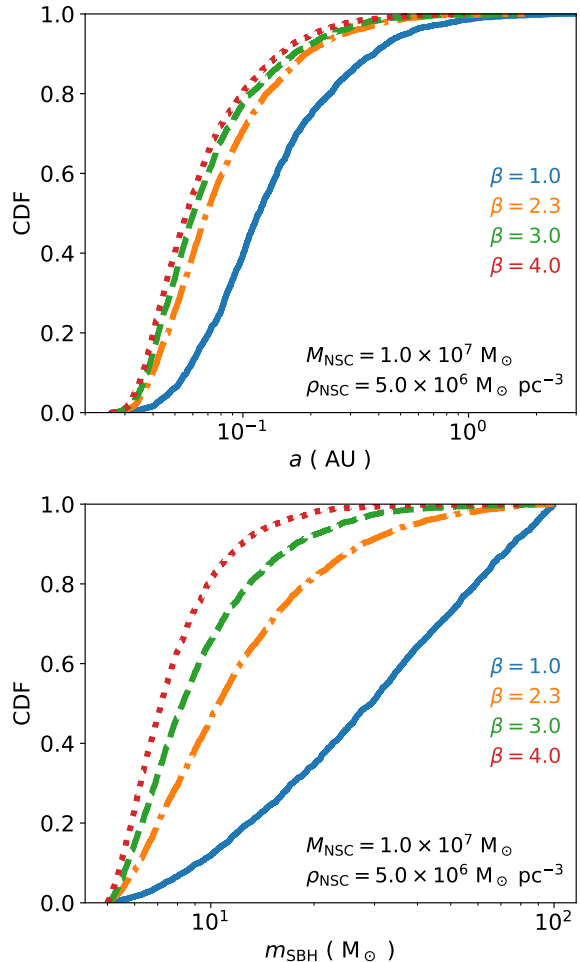


Figure 4. Distribution of semi-major axis (a) of the SBH-SBH binaries (top) and masses (m_{SBH}) of the SBHs (bottom) that undergo a TDE, for different values of the slope of the SBH mass function. The mass and density of the NSC are fixed to $M_{\text{NSC}} = 10^6 M_{\odot}$ and $\rho_{\text{NSC}} = 5 \times 10^6 M_{\odot} \text{pc}^{-3}$, respectively.

range ($a_{\text{GW}}, a_{\text{hard}}$), where

$$a_{\text{GW}} \propto \frac{M_{\text{NSC}}^{1/15}}{\rho_{\text{NSC}}^{1/6}}. \quad (12)$$

Larger densities correspond to smaller values of a_{GW} , thus a wider range of possible binary semi-major axes, while the NSC mass does not have a significant effect.

Figure 4 shows the distribution of semi-major axes (a) of the SBH-SBH binaries (top) and masses (m_{SBH}) of the SBHs (bottom) that undergo a TDE, for different values of the slope of the SBH mass function. The mass and density of the NSC are fixed to $M_{\text{NSC}} = 10^6 M_{\odot}$ and $\rho_{\text{NSC}} = 5 \times 10^6 M_{\odot} \text{pc}^{-3}$, respectively. We find that the typical semi-major axis of the binaries that lead to a TDE are larger for smaller values of β . Shallower BH mass functions (smaller β 's) produce on average more massive BHs, which can form hard binaries at larger separations ($a_{\text{hard}} \propto m_{\text{SBH}}$). The slope of the mass function also obviously affect the mass of the BH that undergoes TDE, producing less massive BHs for steeper mass functions. The NSC mass and density do not affect the SBH mass distribution.

The same trends discussed for SBH-SBH binaries hold for IMBH-SBH and IMBH-IMBH binaries, with the only difference that their typical semi-major axes are larger, being more massive than SBH-SBH binaries.

3.4 Rates

We now turn to the astrophysical rates of stellar TDEs onto binary BHs expected from NSCs. The rate per galaxy depends both on the mass and density of the host NSC and the absolute number of binary BHs (N_{BBH}). A simple "n σ v" calculation leads to,

$$\begin{aligned} \frac{\Gamma_{\text{TDE}}}{\text{gal}} &= N_{\text{BBH}} \nu_{\text{NSC}} \Sigma_{\text{TDE}} \nu_{\text{disp}} = 4.8 \times 10^{-7} \text{ yr}^{-1} \times \\ &\times \left(\frac{\hat{\Sigma}}{0.01} \right) \left(\frac{N_{\text{BBH}}}{100} \right) \left(\frac{m_{\text{BH}}}{30 M_{\odot}} \right)^2 \times \\ &\times \left(\frac{10^5 M_{\odot} \text{ pc}^{-3}}{M_{\text{NSC}}} \right) \left(\frac{\rho_{\text{NSC}}}{10^5 M_{\odot} \text{ pc}^{-3}} \right)^{1/2}. \end{aligned} \quad (13)$$

Here, we have normalized to the typical values of $\hat{\Sigma}$ found in the previous Section and used the mean density (ρ_{NSC}) of the host NSC.

In the previous equation, the number of BBH has been normalized considering a standard [Kroupa \(2001\)](#) IMF. This is true for stellar SBHs only and assuming a single burst of star formation, while NSCs have more complex histories, with episodic star formation and accretion of star clusters that can lead to morphological and structural transformations ([Antonini 2013](#)). Moreover, dynamics may change the number of BBHs over time, for instance ejecting or disrupting some of them. For IMBHs, the numbers are even more unconstrained. A detailed calculation of the TDE rate in NSCs could be obtained, for example, by means of detailed and large N-body simulations of NSCs, similarly to the ones performed for globular clusters in [Kremer et al. \(2019\)](#). This is beyond the scope of the present paper and we leave this investigation to a future study.

Interestingly, this predicted rate is of the same order of other TDE rates predicted in the literature for a number of different SBH and IMBH systems. Mergers of stars with SBHs have been estimated to $10^{-7} - 10^{-9} \text{ yr}^{-1}$ in star clusters ([Kremer et al. 2019](#); [Samsing et al. 2019](#)) and to $10^{-1} - 10^{-4} \text{ yr}^{-1}$ in hierarchical triple systems ([Fragione et al. 2019](#)). Finally, the rates for SMBHs and IMBHs are estimated to be $10^{-4} - 10^{-5} \text{ yr}^{-1}$ ([van Velzen 2018](#)) and $10^{-3} - 10^{-5} \text{ yr}^{-1}$ ([Fragione & Leigh 2018b](#); [Fragione et al. 2018](#)), respectively.

4 ELECTROMAGNETIC SIGNATURES OF TIDAL DISRUPTION EVENTS IN BINARY BLACK HOLES

In this Section, we start with the discussion of a canonical TDE from an isolated BH, and we then extend the discussion to the case of a binary BH-BH.

A star of mass m_* approaching a BH of mass m_{BH} will be torn apart by its tidal forces if the pericenter R_p of its orbit passes within the tidal radius R_T of the BH. In the Newtonian approximation, which is reasonably accurate for

$R_T \gg R_g \equiv Gm_{\text{BH}}/c^2$ (R_g being the BH gravitational radius), this is given by Eq. 10. The strength of the encounter is measured by the extent to which the pericenter of the star penetrates inside the tidal radius of the BH, quantified by the penetration parameter, $\beta_p = R_T/R_p$. The detailed properties of a TDE depend on the magnitude of β_p , varying from a mild disruption for $\beta_p \approx 1$ to an increasingly more violent encounter (and fuller disruption of the star) as β_p increases. Since the different fluid elements comprising the disrupted star are disrupted at different distances from the BH, they will have a spread in binding energy. The disrupted material with positive binding energy is able to escape the gravitational pull of the BH, while the bound gas stream returns, moving on nearly geodesic orbits around the BH.

The timescale t_0 over which the bound debris return to the BH is approximately determined by the time that it takes for the most bound debris to return to the pericenter R_p (with $R_p \sim R_t$),

$$\begin{aligned} t_0 &= \frac{\pi R_T^3}{\sqrt{2Gm_{\text{BH}}R_*^3}} \approx \\ &\approx 9 \times 10^4 \text{ s} \left(\frac{R_T}{R_{\odot}} \right)^3 \left(\frac{R_{\odot}}{R_*} \right)^{3/2} \left(\frac{10^3 M_{\odot}}{m_{\text{BH}}} \right)^{1/2} = \\ &= 9 \times 10^4 \text{ s} \left(\frac{R_*}{R_{\odot}} \right)^{3/2} \left(\frac{m_*}{M_{\odot}} \right)^{-1} \left(\frac{m_{\text{BH}}}{10^3 M_{\odot}} \right)^{1/2}. \end{aligned} \quad (14)$$

Once the first debris reaches the BH, the rate of fallback for the remaining bound debris will depend on their energy distribution with mass. For a flat distribution, which is found in objects which are completely or nearly disrupted, the return rate follows the scaling ([Phinney 1989](#), based on the original argument by [Rees 1988](#)),

$$\dot{M}_{\text{fb}} \sim \frac{M_{\text{fb},0}}{t_0} \left(\frac{t}{t_0} \right)^{-5/3}, \quad (15)$$

where

$$\begin{aligned} \dot{M}_{\text{fb},0} &= \frac{M_{\text{fb},0}}{t_0} \approx 10^{-5} M_{\odot} \text{ s}^{-1} \times \\ &\times \left(\frac{m_*}{1 M_{\odot}} \right)^2 \left(\frac{R_*}{R_{\odot}} \right)^{-3/2} \left(\frac{m_{\text{BH}}}{10 M_{\odot}} \right)^{-1/2} \end{aligned} \quad (16)$$

On the other hand, in the cases for which only partial disruption of the star is achieved, the fallback rate is found to be steeper than $t^{-5/3}$ (e. g. [Guillochon & Ramirez-Ruiz 2013](#)).

Figure 5 shows the distribution of $\dot{M}_{\text{fb},0}$ for different values of the slope of the BH mass function, for SBH-SBH (top), IMBH-SBH (center), and IMBH-IMBH (bottom) binaries. The density and mass of the host NSC are $\rho_{\text{NSC}} = 5 \times 10^6 M_{\odot} \text{ pc}^{-3}$ and $M_{\text{NSC}} = 10^7 M_{\odot}$, respectively. Since $\dot{M}_{\text{fb},0} \propto m_{\text{BH}}^{-1/2}$, steeper BH mass functions (higher β 's) produce larger $\dot{M}_{\text{fb},0}$'s. We find that the distribution of $\dot{M}_{\text{fb},0}$ peaks at $\sim 4 \times 10^{-6} M_{\odot} \text{ s}^{-1}$ and $\sim 1.3 \times 10^{-5} M_{\odot} \text{ s}^{-1}$ for $\beta = 1$ and $\beta = 4$, respectively, for an SBH-SBH binary. In the same way, the distribution of $\dot{M}_{\text{fb},0}$ presents a peak at $\sim 5 \times 10^{-7} M_{\odot} \text{ s}^{-1}$ and $\sim 3 \times 10^{-6} M_{\odot} \text{ s}^{-1}$ for $\beta = 1$ and $\beta = 4$, respectively, for an IMBH-SBH binary. The distributions for IMBH-SBH binaries present peaks similar to the distributions for IMBH-IMBH binaries, with tails up to $\sim 1.3 \times 10^{-5} M_{\odot} \text{ s}^{-1}$. The reason is that most of the TDEs in these binaries are due to the disruption of stars by the

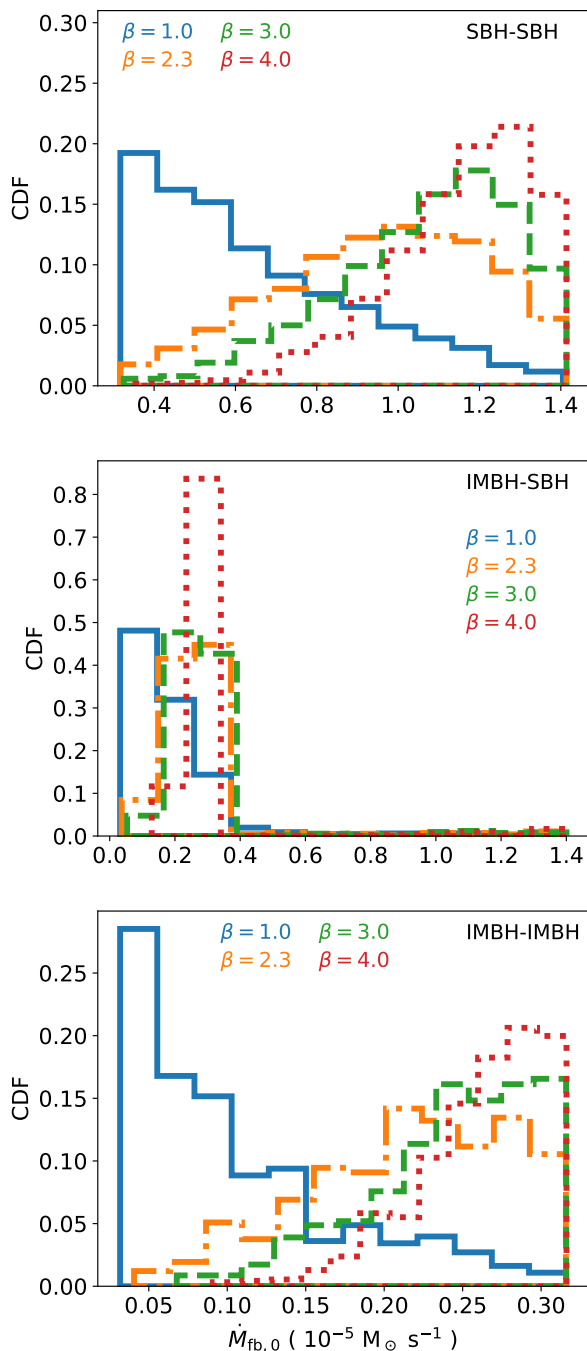


Figure 5. Cumulative distribution functions of $\dot{M}_{\text{fb},0}$ for different values of the slope of the BH mass function, for SBH-SBH (top), IMBH-SBH (center), and IMBH-IMBH (bottom) binaries. The density and mass of the host NSC are assumed to be $\rho_{\text{NSC}} = 5 \times 10^6 M_{\odot} \text{pc}^{-3}$ and $M_{\text{NSC}} = 10^7 M_{\odot}$, respectively.

more massive IMBH, which constitute the bulk of the distribution, while only a few TDEs are due to the SBH, which make up the tails of the distribution.

The detailed evolution of the falling-back bound material is largely determined by its ability to circularize in a disk. For this to happen, the bound matter must lose a significant amount of energy. This is believed to be possible as a result of a combination of effects, such as compression of the

stream at pericenter, thermal viscous and magnetic shears, and the General Relativistic (GR) apsidal precession, which forces highly eccentric debris streams to self-intersect (see i.e. [Chen & Shen 2018](#) for a review of these effects). The issue of whether circularization can be completed before the end of the actual event still remains a matter of debate ([Piran et al. 2015](#)). The energy dissipation due to GR apsidal crossings increases with the BH mass ([Chen & Shen 2018](#)), and can become sufficient to produce circularization. However, for IMBHs and SBHs, this process does not appear to provide enough energy dissipation to lead to circularization. On the other hand, from an observational point of view, the emission from a candidate TDE from an IMBH ([Lin et al. 2018](#)) was found to display evidence for thermal emission, indicative of a thermal thin disk, and hence of efficient circularization. For low-mass BHs, circularization may be aided by the fact that the bound debris are not highly eccentric ([Kremer et al. 2019](#)). Recent hydrodynamical simulations ([Lopez et al. 2019](#)) have found that, for SBHs (with masses in the range of those measured via GWs), energy dissipation via shocks at pericenter can be significant enough to lead to efficient circularization. For simplicity, we continue our discussion assuming that a disk can be promptly formed, but keeping this important caveat in mind.

Once a disk is formed, the timescale for the tidally disrupted debris to accrete is set by the viscous timescale ([Shakura & Sunyaev 1973](#)). For a geometrically thick disk (i.e. with a scale height $H/R \sim 1$), as expected at high accretion rates, this is given by,

$$t_{\text{acc}} \sim \frac{1}{\alpha \Omega_{\text{K}}(R_{\text{in}})} = 4 \times 10^3 \text{ s} \left(\frac{\alpha}{0.1} \right)^{-1} \left(\frac{R_{\text{in}}}{2 R_{\odot}} \right)^{3/2} \left(\frac{m_{\text{BH}}}{10^3 M_{\odot}} \right)^{-1/2}. \quad (17)$$

If the viscous timescale is short compared to the fallback time, then the accretion rate to the BH directly tracks the fallback rate, i.e. $\dot{M}_{\text{acc}} \sim \dot{M}_{\text{fb}}$, otherwise its viscosity slows it down. However, even under these conditions, for typical parameters the early accretion rate is expected to be super-Eddington. Under these conditions, which are commonly observed in both the long and the short gamma-ray bursts (GRBs, e.g. [Popham et al. 1999](#); [Narayan et al. 2001](#); [Janiuk et al. 2004](#)), a relativistic jet could be launched, giving rise to high-energy emission. The maximum accretion rates for SBHs have been estimated to be on the order of $10^{-6} - 10^{-5} M_{\odot} \text{ s}^{-1}$. These values are somewhat comparable to those found in numerical simulations of the collapse of blue supergiant stars ([Perna et al. 2018](#)), which have been proposed as progenitors of the sub-class of very long GRBs ([Gendre et al. 2013](#)). If launched ([Fialkov & Loeb 2017](#)), a relativistic jet would produce high energy radiation (γ -rays and X-rays) over timescales of $10^3 - 10^4$ s. However, even if a relativistic jet is not launched, an outflow is likely to be driven, as demonstrated in both analytical works ([Narayan & Yi 1994](#); [Blandford & Begelman 1999](#)) and in radiation-hydrodynamical simulations ([Dai et al. 2018](#); [Kremer et al. 2019](#)).

Since many TDEs are observed with significant (and often dominant) optical/UV emission, it is believed that this must be produced due to reprocessing of higher-energy radiation at some distance R_{ph} within the outflow (see e.g. [Mockler et al. 2019](#)). To zeroth order, the spectrum is thermal, with an effective temperature at the photosphere

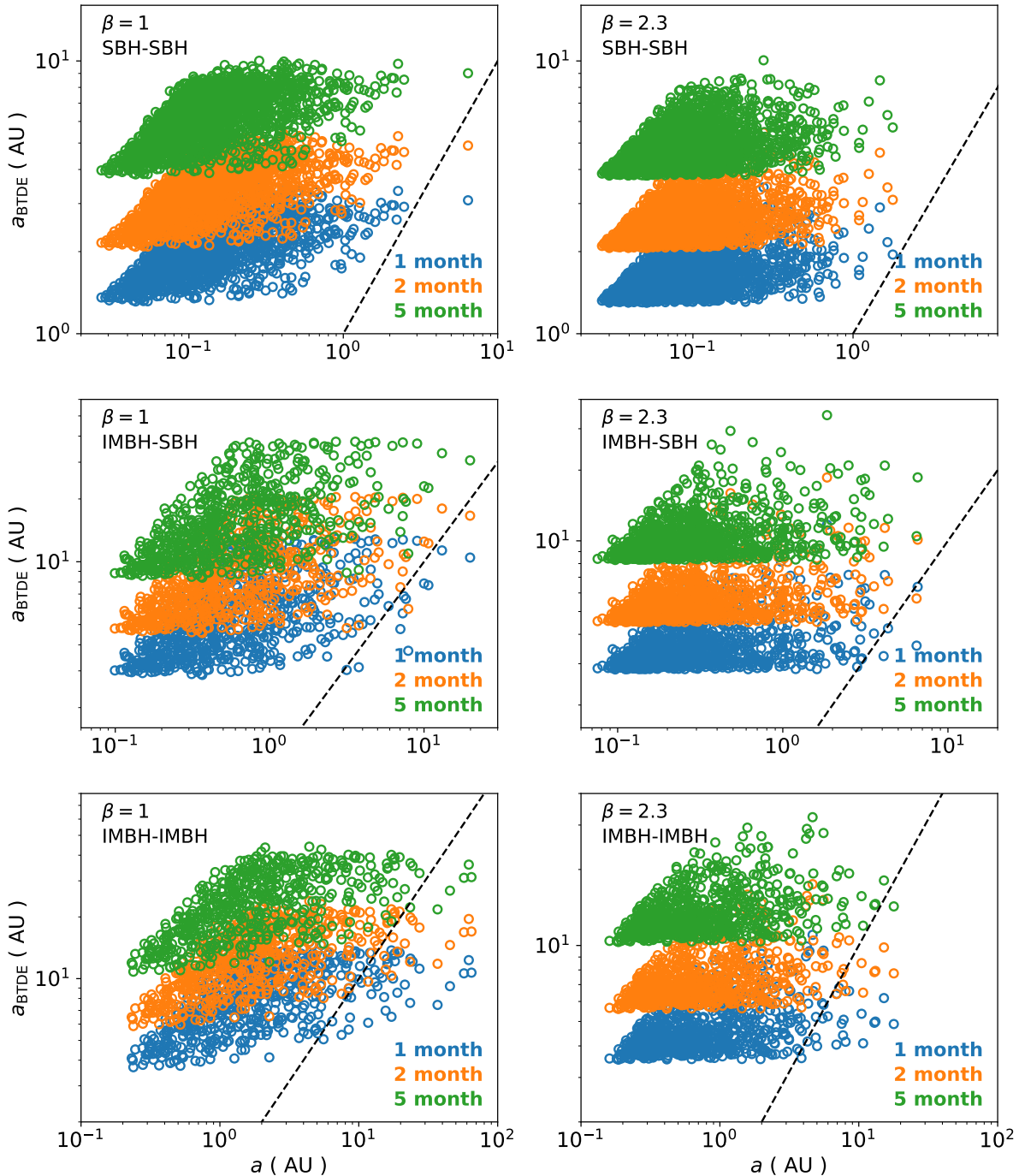


Figure 6. Distribution of the orbital semi-major axis a and a_{BTDE} (Eq. 18) for SBH-SBH (top), IMBH-SBH (center), IMBH-IMBH (bottom) binaries that undergo a TDE. Left: $\beta = 1.0$; right $\beta = 2.3$. The mass and density of the host NSC are assumed to be $M_{\text{NSC}} = 10^6 M_{\odot}$ and $\rho_{\text{NSC}} = 5 \times 10^6 M_{\odot} \text{pc}^{-3}$, respectively. The black-dashed line represents the $x = y$ line. Different colors represent different observation times after the TDE: 1 month (blue), 2 month (orange), 5 month (green).

$T_{\text{ph}} \simeq [L/(4\pi R_{\text{ph}}^2 \sigma)]^{1/4}$. For parameters typical of an IMBH, the spectrum peaks in the UV until the photosphere recedes back to the radius at which the outflow is launched, and later it peaks in the far UV and X-ray bands (Chen & Shen 2018). The outflow luminosity during the super-Eddington phase is not well known. There have been suggestions (e.g. King & Muldrew 2016; Lin et al. 2017) that, for $\dot{M}_{\text{acc}} \gtrsim \dot{M}_{\text{Edd}}$, this luminosity scales logarithmically with \dot{M}_{acc} , while some nu-

merical simulations of super-Eddington accretion disks indicate that, under the presence of strong magnetic fields ($\sim 10^3$ G), the wind luminosity can be substantially larger than the Eddington value (Sadowski & Narayan 2016). For an IMBH of $\sim 10^4 M_{\odot}$, the super-Eddington phase lasts for over ~ 10 years (e.g., Chen & Shen 2018), but it is shorter for smaller masses ($t(\dot{M}) \propto m_{\text{BH}}^{1/2}$ (e.g., Mockler et al. 2019)).

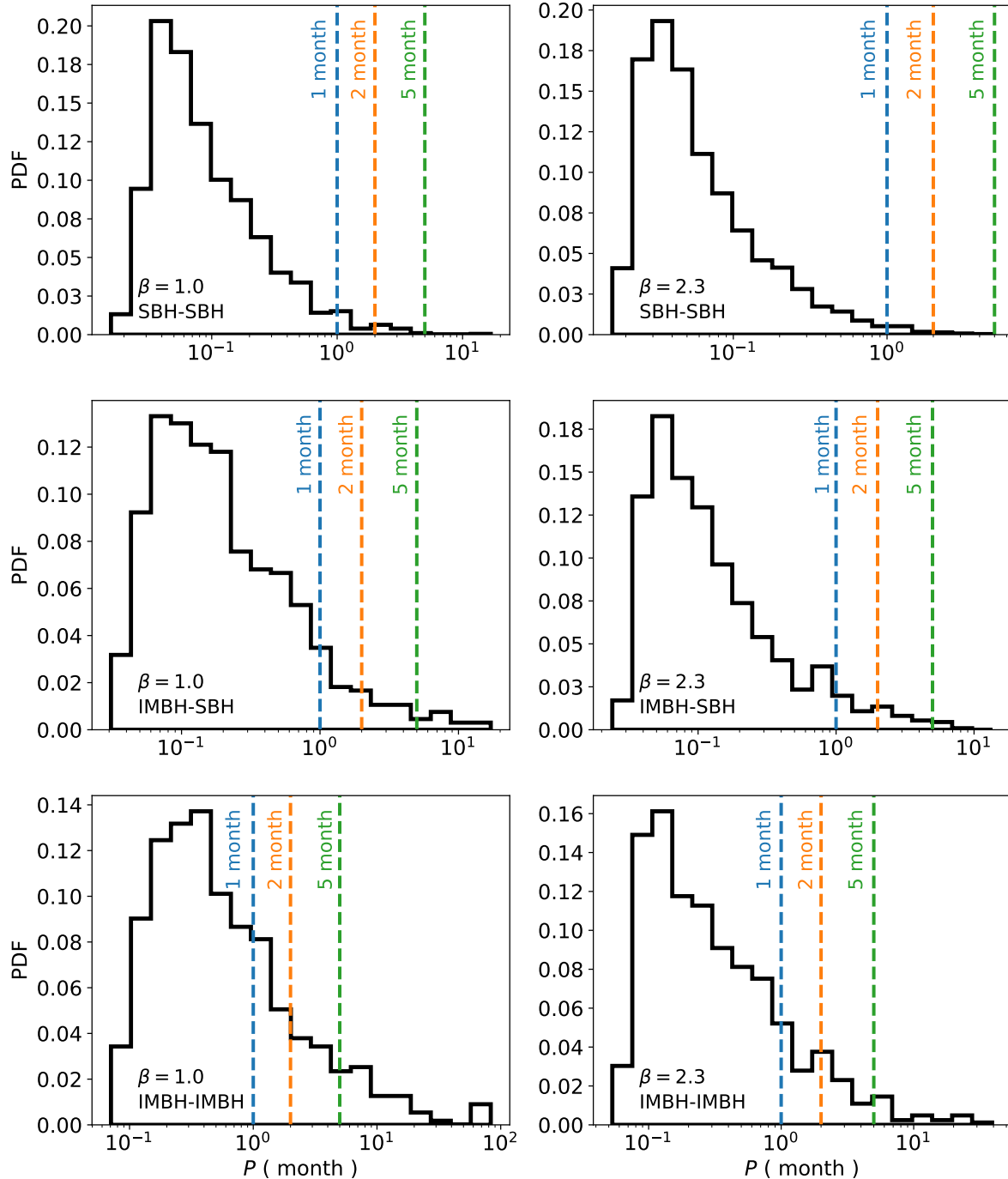


Figure 7. Probability distribution function of the orbital periods P for SBH-SBH (top), IMBH-SBH (center), IMBH-IMBH (bottom) binaries that undergo a TDE. Left: $\beta = 1.0$; right $\beta = 2.3$. The mass and density of the host NSC are $M_{\text{NSC}} = 10^6 M_{\odot}$ and $\rho_{\text{NSC}} = 5 \times 10^6 M_{\odot} \text{pc}^{-3}$, respectively. The colored-dashed lines represent different observation times after the TDE: 1 month (blue), 2 month (orange), 5 month (green).

The radiation-hydrodynamic calculations by [Kremer et al. \(2019\)](#) show that, for a representative BH of $20M_{\odot}$, the outflow can give rise to optical transients $\sim 10^{42} - 10^{44} \text{ erg s}^{-1}$ (with the different values mostly dependent on the mass outflow rate), from timescales of a few hours to a few days, slowly declining down to luminosities on the order of a few $\times 10^{40}$ – a few $\times 10^{42} \text{ erg s}^{-1}$ over a timescale of about 100 days. Once the accretion rate becomes sub-Eddington, the

outflow is likely quenched, and the luminosity scales with the accretion rate, eventually becoming sub-dominant with respect to the luminosity of the accretion disk, as \dot{M}_{acc} declines.

All the above considerations strictly hold for the case of a TDE onto an isolated BH, or for the case in which, if the BH is part of a binary, the companion BH does not perturb the dynamics of the TDE stream ([Hayasaki & Loeb 2016](#)).

The required conditions for this to be the case, and the modifications in case of influence by the secondary, are discussed in the following (see Coughlin et al. 2019, for a review). The dynamics of the fallback debris will be drastically altered if the relative magnitudes of the apocenter distance R_p and the binary separation a are such that $R_p > a/2$. At time T after the disruption, this translates into the condition,

$$a \lesssim a_{\text{BTDE}} \approx 6 \left(\frac{M}{10^3 M_\odot} \right)^{1/3} \left(\frac{T}{1 \text{ month}} \right)^{2/3} \text{ AU}. \quad (18)$$

Given the typical tight separations of our BH-BH binaries, dictated by the high masses and densities of the host NSCs, it is evident that binarity will influence the TDEs discussed in this work.

We illustrate the effect of the secondary BH in Figure 6, where we plot the distribution of the orbital semi-major axis a and a_{BTDE} for SBH-SBH (top), IMBH-SBH (center), IMBH-IMBH (bottom) binaries that undergo a TDE, in a NSC of mass and density of $M_{\text{NSC}} = 10^6 M_\odot$ and $\rho_{\text{NSC}} = 5 \times 10^6 M_\odot \text{ pc}^{-3}$, respectively. Since typically SBH-SBH binaries need to be tighter than IMBH-SBH and IMBH-IMBH binaries to be hard binaries in a NSC environment (Eq. 2), the dynamics of the fallback debris is likely to be perturbed by the secondary in a larger number of cases. We find that most of the SBH-SBH binaries that undergo a TDE present this effect within ~ 1 month after the TDE. On the other hand, IMBH-SBH and IMBH-IMBH binaries can show signatures of binarity on longer timescales after the TDE, owing to their typical larger separations. We show in Figure 7 the probability distribution function of the orbital periods P for SBH-SBH (top), IMBH-SBH (center), IMBH-IMBH (bottom) binaries that undergo a TDE, presented in the Figure 6. Most of the systems have orbital periods smaller than a few months, implying that the modulation of the tidal debris due to the companion BH can be imprinted in the signal.

Simulations of SBHs (in the LIGO/Virgo range) by Lopez et al. (2019) have shown that, for $R_t > a$, the binary BH ends up embedded in a circumbinary disk which accretes on both BHs on the viscous timescale. This situation would hence likely lead to a transient similar to what discussed in the case of a single BH. If the two BHs have unequal mass, such as in the case of an IMBH-SBH binary, the accretion luminosity would be dominated by that of the larger BH. As discussed, a different outcome can arise if $R_t \lesssim a$. In this case the disruption is dominated by the primary BH (closer to the star), but the detailed later dynamics of the debris is influenced by the secondary BH by an amount which depends on the orbital separation. Lopez et al. (2019) quantified this via a_{90} , that is the semi-major axis of the material which contains 90% of the mass, as measured inwards from the most bound star material. If $a_{90} < R_L$, where R_L is the Roche lobe radius of the disrupting BH (Eggleton 1983), then most of the debris will accrete onto the primary BH, with only a small perturbation by the secondary one, and hence the TDE will be similar to that of the isolated BH discussed above. On the other hand, if $a_{90} \gtrsim R_L$, the tidal debris will be affected by the presence of the secondary BH, and accrete onto it, giving rise to more complex light curves, whose detailed shape depends on several parameters, including the mass ratio of the BHs in the binary. However, peak accretion rates are still found to be of the same order of

magnitude as for the isolated BH case, hence leading confidence to the observability of TDE events under a wide range of conditions. It should be noted, however, that extracting the masses of the BHs in the case in which both contribute to the TDE will be significantly more difficult with respect to the case in which the TDE event is dominated by a single BH (Mockler et al. 2019).

The next decade is expected to be transformative for transient astronomy, and especially so for TDEs, with the upcoming optical surveys, and in particular the Zwicky Transient Facility (ZTF)⁶ and LSST⁷. An event with an optical luminosity of $\sim 10^{42} \text{ erg s}^{-1}$ can be detected by ZTF up to a distance of about 150 Mpc. However, the major observational breakthrough for TDEs is expected with LSST, which will be sensitive to an event of luminosity $\sim 10^{42} \text{ erg s}^{-1}$ up to a distance of ~ 0.5 Gpc with 15 s of integration time in standard routine sky scans in the r band (yielding a limiting magnitude of $r \sim 24.5$).

5 CONCLUSIONS

We have discussed the electromagnetic signature of TDEs of stars through the assembly and merger of binary SBHs and IMBHs in NSCs. The lightcurve of these TDEs could be interrupted and modulated by the companion BH on the orbital period of the binary (Liu et al. 2009; Coughlin et al. 2017; Fragione et al. 2019), enabling to probe their orbital period distribution (Samsing et al. 2019). We have explored in detail the dynamics that drive stars in NSCs to be tidally disrupted by SBH-SBH, IMBH-IMBH, and IMBH-IMBH binaries. We have shown that the orbital properties and the masses of the binaries that exhibit a TDE are set by the NSC mass and density and by the slope of the BH mass function.

For typical NSC properties, we have estimated a merger rate of $\sim 10^{-6}$ – 10^{-7} yr^{-1} per galaxy, which is similar to other TDE rates predicted in literature for a number of different SBH and IMBH system, including TDEs in star clusters (Kremer et al. 2019; Samsing et al. 2019), in hierarchical triple systems (Fragione et al. 2019), and onto SMBHs in galactic nuclei (van Velzen 2018) and IMBHs both in galactic nuclei and star clusters (Fragione & Leigh 2018b; Fragione et al. 2018).

The ejected mass associated with these TDEs could produce optical transients of luminosity $\sim 10^{42}$ – $10^{44} \text{ erg s}^{-1}$ with timescales of order a day to a month. These events should be detectable by optical transient surveys, such as ZTF and LSST.

Present and upcoming GW detectors promise to detect hundreds of merging SBHs and IMBHs over the next decade. The origin and distribution of these SBH and IMBH binaries in dynamical environments is a fundamental and a key scientific question that will be addressed by the forthcoming data. TDEs offer a unique insight into dynamically assembled binaries in the dense environments of NSCs, where the effect of binarity can be detected within only a few weeks up to a few months. Moreover, they

⁶ <https://www.ztf.caltech.edu/>

⁷ <https://www.lsst.org/lsst/>

provide a unique probe of the elusive population of IMBHs, which could be difficult to trace through other observations. As new electromagnetic surveys, such as ZTF and LSST, improve and start operating, a large number of TDEs is expected to be observed, rendering these transients excellent probes of the SBH and IMBH populations in galactic nuclei.

Data Availability

The data underlying this article will be shared on reasonable request to the corresponding author.

ACKNOWLEDGEMENTS

GF acknowledges support from a CIERA postdoctoral fellowship at Northwestern University. RP acknowledges support from NSF award AST-1616157. AL was supported in part by the Black Hole initiative at Harvard University, which is funded by JTF and GBMF grants.

REFERENCES

- Amaro-Seoane P., Gair J. R., Freitag M., Miller M. C., Mandel I., Cutler C. J., Babak S., 2007, *Classical and Quantum Gravity*, 24, R113
- Antognini J. M. O., Thompson T. A., 2016, *MNRAS*, 456, 4219
- Antonini F., 2013, *ApJ*, 763, 62
- Antonini F., Gieles M., Gualandris A., 2019, *MNRAS*, 486, 5008
- Antonini F., Perets H. B., 2012, *ApJ*, 757, 27
- Antonini F., Rasio F. A., 2016, *ApJ*, 831, 187
- Antonini F., Toonen S., Hamers A. S., 2017, *ApJ*, 841, 77
- Arca-Sedda M., Gualandris A., 2018, *MNRAS*, 477, 4423
- Askar A., Szkudlarek M., Gondek-Rosińska D., Giersz M., Bulik T., 2017, *MNRAS*, 464, L36
- Banerjee S., 2018, *MNRAS*, 473, 909
- Bartos I., Kocsis B., Haiman Z., Márka S., 2017, *ApJ*, 835, 165
- Belczynski K., Holz D. E., Bulik T., O’Shaughnessy R., 2016, *Nature*, 534, 512
- Bellovary J., Brooks A., Colpi M., Eracleous M., Holley-Bockelmann K., Hornschemeier A., Mayer L., Natarajan P., Slutsky J., Tremmel M., 2019, *BAAS*, 51, 175
- Blandford R. D., Begelman M. C., 1999, *MNRAS*, 303, L1
- Bromm V., 2013, *Reports on Progress in Physics*, 76, 112901
- Bromm V., Larson R. B., 2004, *ARA& A*, 42, 79
- Capuzzo-Dolcetta R., Miocchi P., 2008, *MNRAS*, 388, L69
- Capuzzo-Dolcetta R., Tosta e Melo I., 2017, *MNRAS*, 472, 4013
- Chen J.-H., Shen R.-F., 2018, *ApJ*, 867, 20
- Chen X., Madau P., Sesana A., Liu F. K., 2009, *ApJL*, 697, L149
- Chen X., Sesana A., Madau P., Liu F. K., 2011, *ApJ*, 729, 13
- Côté P., Piatek S., Ferrarese L., Jordán A., Merritt D., Peng E. W., Haşegan M., Blakeslee J. P., Mei S., West M. J., Milosavljević M., Tonry J. L., 2006, *ApJS*, 165, 57
- Coughlin E. R., Armitage P. J., Lodato G., Nixon C. J., 2019, *Space Sci. Rev.*, 215, 45
- Coughlin E. R., Armitage P. J., Nixon C., Begelman M. C., 2017, *MNRAS*, 465, 3840
- Dai L., McKinney J. C., Roth N., Ramirez-Ruiz E., Miller M. C., 2018, *ApJL*, 859, L20
- Di Carlo U. N., Giacobbo N., Mapelli M., Pasquato M., Spera M., Wang L., Haardt F., 2019, *MNRAS*, 487, 2947
- Di Carlo U. N., Mapelli M., Giacobbo N., Spera M., Bouffanais Y., Rastello S., Santoliquido F., Pasquato M., Ballone A. r., Trani A. A., Torniamenti S., Haardt F., 2020, *arXiv e-prints*, p. arXiv:2004.09525
- Eggleton P. P., 1983, *ApJ*, 268, 368
- Fialkov A., Loeb A., 2017, *MNRAS*, 471, 4286
- Fragione G., Bromberg O., 2019, *MNRAS*, 488, 4370
- Fragione G., Ginsburg I., Kocsis B., 2018, *ApJ*, 856, 92
- Fragione G., Grishin E., Leigh N. W. C., Perets H. B., Perna R., 2019, *MNRAS*, 488, 47
- Fragione G., Kocsis B., 2018a, *Phys Rev Lett*, 121, 161103
- Fragione G., Kocsis B., 2018b, *Phys Rev Lett*, 121, 161103
- Fragione G., Kocsis B., 2019, *MNRAS*, 486, 4781
- Fragione G., Leigh N., 2018a, *MNRAS*, 480, 5160
- Fragione G., Leigh N., 2018b, *MNRAS*, 479, 3181
- Fragione G., Leigh N. W. C., Ginsburg I., Kocsis B., 2018, *ApJ*, 867, 119
- Fragione G., Leigh N. W. C., Perna R., Kocsis B., 2019, *MNRAS*, 489, 727
- Fragione G., Loeb A., Kremer K., Rasio F. A., 2020, *arXiv e-prints*, p. arXiv:2002.02975
- Fragione G., Silk J., 2020, *arXiv e-prints*, p. arXiv:2006.01867
- Fregeau J. M., Cheung P., Portegies Zwart S. F., Rasio F. A., 2004, *MNRAS*, 352, 1
- Fryer C. L., Woosley S. E., Heger A., 2001, *ApJ*, 550, 372
- Gendre B., Stratta G., Atteia J. L., Basa S., Boër M., Coward D. M., Cutini S., D’Elia V., Howell E. J., Klotz A., Piro L., 2013, *ApJ*, 766, 30
- Georgiev I. Y., Böker T., 2014, *MNRAS*, 441, 3570
- Georgiev I. Y., Böker T., Leigh N., Lützgendorf N., Neumayer N., 2016, *MNRAS*, 457, 2122
- Georgiev I. Y., Hilker M., Puzia T. H., Goudfrooij P., Baumgardt H., 2009, *MNRAS*, 396, 1075
- Giacobbo N., Mapelli M., 2018, *MNRAS*, 480, 2011
- Giersz M., Leigh N. W., Hypki A., Lützgendorf N., Askar A., 2015, *MNRAS*, 454, 3150
- Gnedin O. Y., Ostriker J. P., Tremaine S., 2014, *ApJ*, 785, 71
- Grishin E., Perets H. B., Fragione G., 2018, *MNRAS*, 481, 4907
- Guillochon J., Ramirez-Ruiz E., 2013, *ApJ*, 767, 25
- Gürkan M. A., Freitag M., Rasio F. A., 2004, *ApJ*, 604, 632
- Gürkan M. A., Rasio F. A., 2005, *ApJ*, 628, 236
- Hamers A. S., Thompson T. A., 2019, *ApJ*, 883, 23
- Hamilton C., Rafikov R. R., 2019, *arXiv e-prints*, p. arXiv:1907.00994
- Hayasaki K., Loeb A., 2016, *Scientific Reports*, 6, 35629
- Heggie D. C., 1975, *Mon. Not. R. Astron. Soc*, 173, 729
- Janiuk A., Perna R., Di Matteo T., Czerny B., 2004, *MNRAS*, 355, 950
- King A., Muldrew S. I., 2016, *MNRAS*, 455, 1211
- Kremer K., Lu W., Rodriguez C. L., Lachat M., Rasio

- F. A., 2019, *ApJ*, 881, 75
- Kremer K., Spera M., Becker D., Chatterjee S., Di Carlo U. N., Fragione G., Rodriguez C. L., Ye C. S., Rasio F. A., 2020, arXiv e-prints, p. arXiv:2006.10771
- Kremer K., Ye C. S., Rui N. Z., Weatherford N. C., Chatterjee S., Fragione G., Rodriguez C. L., Spera M., Rasio F. A., 2020, *ApJS*, 247, 48
- Kroupa P., 2001, *MNRAS*, 322, 231
- Kruckow M. U., Tauris T. M., Langer N., Kramer M., Izzard R. G., 2018, *MNRAS*, 481, 1908
- Lee H. M., 1995, *MNRAS*, 272, 605
- LIGO/Virgo Scientific Collaboration 2019a, *Physical Review X*, 9, 031040
- LIGO/Virgo Scientific Collaboration 2019b, *Phys. Rev. D*, 100, 064064
- LIGO/Virgo Scientific Collaboration 2020a, arXiv e-prints, p. arXiv:2004.08342
- LIGO/Virgo Scientific Collaboration 2020b, *ApJL*, 892, L3
- Lin D., Guillochon J., Komossa S., Ramirez-Ruiz E., Irwin J. A., Maksym W. P., Grupe D., Godet O., Webb N. A., Barret D., Zauderer B. A., Duc P.-A., Carrasco E. R., Gwyn S. D. J., 2017, *Nature Astronomy*, 1, 0033
- Lin D., Strader J., Carrasco E. R., Page D., Romanowsky A. J., Homan J., Irwin J. A., Remillard R. A., Godet O., Webb N. A., Baumgardt H., Wijnands R., Barret D., Duc P.-A., Brodie J. P., Gwyn S. D. J., 2018, *Nature Astronomy*, 2, 656
- Liu B., Lai D., 2019, *MNRAS*, 483, 4060
- Liu F. K., Li S., Chen X., 2009, *ApJL*, 706, L133
- Loeb A., Furlanetto S. R., 2013, *The First Galaxies in the Universe*
- Lopez Martin J., Batta A., Ramirez-Ruiz E., Martinez I., Samsing J., 2019, *ApJ*, 877, 56
- Madau P., Rees M. J., 2001, *ApJL*, 551, L27
- Mandel I., Brown D. A., Gair J. R., Miller M. C., 2008, *ApJ*, 681, 1431
- Mastrobuono-Battisti A., Perets H. B., Loeb A., 2014, *ApJ*, 796, 40
- McKernan B., Ford K. E. S., Kocsis B., Lyra W., Winter L. M., 2014, *MNRAS*, 441, 900
- McKernan B., Ford K. E. S., Lyra W., Perets H. B., 2012, *MNRAS*, 425, 460
- McKernan B., Ford K. E. S., O’Shaughnessy R., Wysocki D., 2019, arXiv e-prints, p. arXiv:1907.04356
- Miller M. C., 2009, *Classical and Quantum Gravity*, 26, 094031
- Miller M. C., Lauburg V. M., 2009, *ApJ*, 692, 917
- Mockler B., Guillochon J., Ramirez-Ruiz E., 2019, *ApJ*, 872, 151
- Narayan R., Piran T., Kumar P., 2001, *ApJ*, 557, 949
- Narayan R., Yi I., 1994, *ApJL*, 428, L13
- O’Leary R. M., Kocsis B., Loeb A., 2009, *MNRAS*, 395, 2127
- Pechetti R., Seth A., Neumayer N., Georgiev I., Kacharov N., den Brok M., 2020, *ApJ*, 900, 32
- Perna R., Lazzati D., Cantiello M., 2018, *ApJ*, 859, 48
- Perna R., Wang Y.-H., Farr W. M., Leigh N., Cantiello M., 2019, *ApJL*, 878, L1
- Phinney E. S., 1989, in Morris M., ed., *The Center of the Galaxy Vol. 136 of IAU Symposium, Manifestations of a Massive Black Hole in the Galactic Center*. p. 543
- Piran T., Svirski G., Krolik J., Cheng R. M., Shiokawa H., 2015, *ApJ*, 806, 164
- Popham R., Woosley S. E., Fryer C., 1999, *ApJ*, 518, 356
- Portegies Zwart S. F., McMillan S. L. W., 2002, *ApJ*, 576, 899
- Quinlan G. D., 1996, *New A*, 1, 35
- Rasskazov A., Fragione G., Kocsis B., 2019, arXiv e-prints, p. arXiv:1912.07681
- Rasskazov A., Fragione G., Leigh N. W. C., Tagawa H., Sesana A., Price-Whelan A., Rossi E. M., 2019, *ApJ*, 878, 17
- Rasskazov A., Kocsis B., 2019, *ApJ*, 881, 20
- Rees M. J., 1988, *Nature*, 333, 523
- Rodriguez C. L., Amaro-Seoane P., Chatterjee S., Rasio F. A., 2018, *PRL*, 120, 151101
- Sadowski A., Narayan R., 2016, *MNRAS*, 456, 3929
- Samsing J., 2018, *Phys. Rev. D*, 97, 103014
- Samsing J., D’Orazio D. J., Kremer K., Rodriguez C. L., Askar A., 2019, arXiv e-prints, p. arXiv:1907.11231
- Samsing J., Venumadhav T., Dai L., Martinez I., Batta A., Lopez M., Ramirez-Ruiz E., Kremer K., 2019, *Phys. Rev. D*, 100, 043009
- Secunda B., et al., 2018, ArXiv e-prints
- Shakura N. I., Sunyaev R. A., 1973, *A&A*, 24, 337
- Silsbee K., Tremaine S., 2017, *ApJ*, 836, 39
- Tagawa H., Haiman Z., Kocsis B., 2019, arXiv e-prints, p. arXiv:1909.10517
- Tremaine S. D., Ostriker J. P., Spitzer L. J., 1975, *ApJ*, 196, 407
- Turner M., 1977, *ApJ*, 216, 610
- Turner M. L., Côté P., Ferrarese L., Jordán A., Blakeslee J. P., Mei S., Peng E. W., West M. J., 2012, *ApJS*, 203, 5
- van Velzen S., 2018, *ApJ*, 852, 72
- Yang Y., Bartos I., Gayathri V., Ford K. E. S., Haiman Z., Klimentenko S., Kocsis B., Márka S., Márka Z., McKernan B., O’Shaughnessy R., 2019, *Phys Rev Lett*, 123, 181101